A Simple Analytical Model for Understanding the Formation of Sea Surface Temperature Patterns under Global Warming*

LEI ZHANG

Department of Atmospheric Sciences, University of Hawai'i at Mānoa, Honolulu, Hawaii

TIM LI

Department of Atmospheric Sciences, University of Hawai'i at Mānoa, Honolulu, Hawaii, and Climate Dynamics Research Center/Earth System Modeling Center, International Laboratory on Climate and Environment Change, Nanjing University of Information Science and Technology, Nanjing, China

(Manuscript received 13 May 2014, in final form 12 August 2014)

ABSTRACT

How sea surface temperature (SST) changes under global warming is critical for future climate projection because SST change affects atmospheric circulation and rainfall. Robust features derived from 17 models of phase 5 of the Coupled Model Intercomparison Project (CMIP5) include a much greater warming in high latitudes than in the tropics, an El Niño–like warming over the tropical Pacific and Atlantic, and a dipole pattern in the Indian Ocean. However, the physical mechanism responsible for formation of such warming patterns remains open.

A simple theoretical model is constructed to reveal the cause of the future warming patterns. The result shows that a much greater polar, rather than tropical, warming depends primarily on present-day mean SST and surface latent heat flux fields, and atmospheric longwave radiation feedback associated with cloud change further enhances this warming contrast. In the tropics, an El Niño–like warming over the Pacific and Atlantic arises from a similar process, while cloud feedback resulting from different cloud regimes between east and west ocean basins also plays a role. A dipole warming over the equatorial Indian Ocean is a response to weakened Walker circulation in the tropical Pacific.

1. Introduction

Because of anthropogenic activities, CO_2 concentration in the atmosphere has increased rapidly since the Industrial Revolution. Because of the greenhouse gas effect, more longwave radiation is trapped within the earth system, leading to a higher global mean surface temperature. Although the distribution of CO_2 increase is rather uniform, the SST warming patterns simulated by state-of-the-art coupled atmosphere–ocean models are nonuniform, which have great impacts on regional weather and climate projection (e.g., Allen and Ingram 2002; Vecchi et al. 2008; Li et al. 2010; Murakami and Wang 2010; Zhao and Held 2010, 2012). Figure 1 shows the ensemble mean of SST warming pattern simulated by 17 models from phase 5 of the Coupled Model Intercomparison Project (CMIP5), using representative concentration pathway 4.5 (RCP4.5). The greatest warming appears over the Arctic Ocean (called polar amplification), and the equatorial warming is slightly larger than that in the subtropics. Along the equator, an El Niño–like warming pattern appears in the tropical Pacific and Atlantic, while a dipole-like pattern occurs in the tropical Indian Ocean (IO).

Polar amplification is commonly attributed to sea ice–albedo positive feedback. Under global warming, sea ice cover in the polar region decreases because of higher surface temperature. This leads to smaller albedo of the surface and thus less reflection of downward solar radiation, which warms the ocean further. However, numerical

* School of Ocean and Earth Science and Technology Contribution Number 9191, International Pacific Research Center Contribution Number 1073, and Earth System Modeling Center Contribution Number 015.

Corresponding author address: Tim Li, IPRC and Department of Atmospheric Sciences, University of Hawaii, 1680 East-West Rd., Post 409B, Honolulu, HI 96822.
E-mail: timli@hawaii.edu

DOI: 10.1175/JCLI-D-14-00346.1

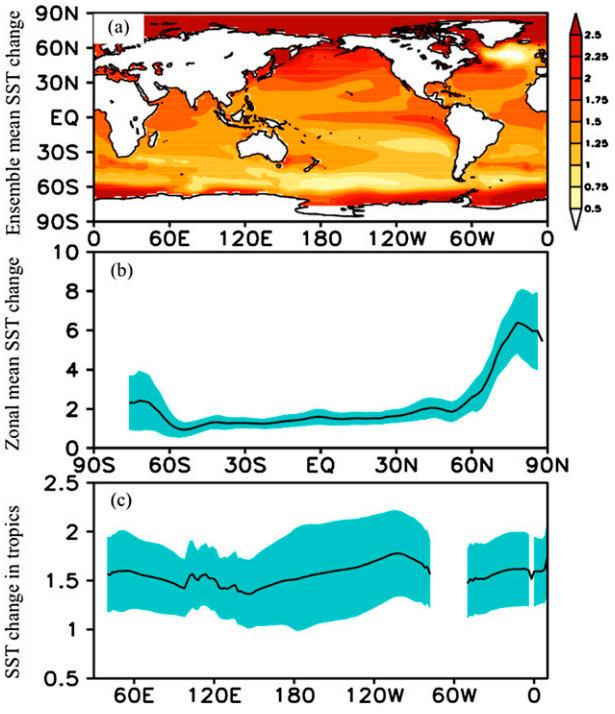

FIG. 1. (a) Ensemble mean of SST change patterns (K) in 17 CMIP5 models. Shown is global warming minus present day value. (b) Black line is the zonal mean SST changes, and shading stands for the uncertainty among different models. (c) Black line is the SST changes averaged between 5°S and 5°N, and shading shows the uncertainty of the zonal SST changes among the 17 models (one std dev across the models).

experiments showed that a greater warming in the Arctic Ocean happened even without sea ice feedback effects (Alexeev 2003; Alexeev et al. 2005). This motivates us to investigate other mechanisms for polar amplification.

It has been shown that, consistent with reduced east–west SST gradient in the tropical Pacific, the Walker circulation is weakened in most of the climate model projections (Hsu and Li 2012; Liu et al. 2013; Ma et al. 2012; Vecchi et al. 2006; Vecchi and Soden 2007; Xie et al. 2010). The weakening of the Walker circulation has been attributed to a slower rate of increase in global mean precipitation than in moisture (Held and Soden 2006). An alternative argument is that the atmosphere becomes more stable because of a greater warming in the upper troposphere due to deeper convection, which may weaken the atmospheric ascending motion (Knutson and Manabe 1995). From an oceanic dynamics point view, Clement et al. (1996) argued that a La Niña–like warming pattern would arise because of the vertical advection of a stronger stratification of the upper ocean under global warming.

In this study, by constructing a simple surface heat budget model that utilizes simulation results from 17 CMIP5 models, we will demonstrate that the future warming patterns described in Figs. 1b and 1c are, to a large extent, determined by the present-day climate mean state and modulated by atmospheric wind, moisture, and temperature changes.

2. Model description and methodology

Seventeen CMIP5 model outputs were used for the current analysis. The leading reason to use only 17 model outputs is that variables we intended to analyze (e.g., separate upward and downward longwave radiation) were not available from all models at the time of this analysis. Another reason was limited disk space. Because of these reasons, we could only analyze 17 CMIP5 models (see Table 1 for a list of these models). It has been shown by some previous studies (e.g., Vecchi and Soden 2007; Pithan and Mauritsen 2014) that the basic features of SST warming patterns were quite similar among CMIP models. Monthly surface temperature, surface heat fluxes, surface wind, air temperature, and specific humidity in the troposphere from the models listed in Table 1 are analyzed. Clear-sky downward longwave radiation and shortwave radiation at the surface are available from 13 of 17 models listed in Table 1 (marked by asterisks), which are also analyzed. All the variables are derived from table ''Amon'' in the CMIP5 output, where surface temperature denotes SST at the open sea. Model outputs from RCP4.5, in which the radiative forcing reaches 4.5 W m^{-2} (equivalent to 650 ppm CO_2 concentration) in 2100 and stabilizes after that, are used to examine future SST changes under global warming. The present-day climate state is derived from 20-yr historical simulations (1986–2005). The future warming climate state is derived from another 20-yr period (2081–2100). The difference between the two periods represents the global warming–induced change. To reduce the internal noise of the climate system and more clearly derive the forced signal, we take a multimodel ensemble analysis approach. All analyses in this paper are carried out using RCP4.5 outputs. The RCP8.5 experiment is also examined, and we find that the results are generally similar to those derived from RCP4.5 (not shown).

Assume that both the present-day and future climate states are approximately in an equilibrium state, following Xie et al. (2010). Thus, the future change of surface net heat flux (δQ_{net}) is balanced by the future change of three-dimensional oceanic temperature advection (δD_0):

$$\delta Q_{\text{net}} + \delta D_0 = 0, \tag{1}$$

TABLE 1. The 17 CMIP5 climate models used in this study. Monthly-mean outputs are analyzed for each model, including SST, horizontal winds, surface heat fluxes, specific humidity, surface wind speed, air temperature, and total cloud cover. Asterisks denote the models where clear-sky downward longwave radiation and shortwave radiation at the surface were available.

Model acronym	Full model name	Institute ID	Modeling center (Group)
CCSM4*	Community Climate System Model, version 4	NCAR	National Center for Atmospheric Research
CESM1 (BGC)*	Community Earth System Model, version 1 (Biogeochemistry)		
CESM1-CAM5	Community Earth System Model, version 1 (Community Atmosphere Model, version 5)		
CMCC-CM	CMCC Climate Model	CMCC	Centro Euro-Mediterraneo sui Cambiamenti Climatici
CMCC-CMS	CMCC Coupled Modeling System		
CNRM-CM5*	CNRM Coupled Global Climate Model, version 5	CNRM/CERFACS	Centre National de Recherches Météorologiques (CNRM)/Centre Européen de Recherche et Formation Avancée en Calcul Scientifique (CERFACS)
CanESM2*	Second Generation Canadian Earth System Model	CCCma	Canadian Centre for Climate Modelling and Analysis
FGOALS-g2	Flexible Global Ocean–Atmosphere–Land System Model gridpoint, version 2	LASG-IAP	National Key Laboratory of Numerical Modeling for Atmospheric Sciences and Geophysical Fluid Dynamics (LASG), Institute of Atmospheric Physics (IAP), Chinese Academy of Sciences
IPSL-CM5A-LR*	IPSL Coupled Model, version 5A, low resolution	IPSL	L'Institut Pierre-Simon Laplace
IPSL-CM5A-MR*	IPSL Coupled Model, version 5A, mid resolution		
IPSL-CM5B-LR*	IPSL Coupled Model, version 5B, low resolution		
MIROC-ESM*	Model for Interdisciplinary Research on Climate (MIROC), Earth System Model	MIROC	Japan Agency for Marine-Earth Science and Technology (JAMSTEC), Atmosphere and Ocean Research Institute (The University of Tokyo), and National Institute for Environmental Studies (NIES)
MIROC-ESM-CHEM*	MIROC, Earth System Model, Chemistry coupled		
MIROC5*	MIROC, version 5	MIROC	Atmosphere and Ocean Research Institute (The University of Tokyo), NIES, and JAMSTEC
MPI-ESM-LR*	MPI Earth System Model, low resolution	MPI-M	Max Planck Institute (MPI) for Meteorology
MPI-ESM-MR*	MPI Earth System Model, medium resolution		
MRI-CGCM3*	MRI Coupled Atmosphere–Ocean General Circulation Model, version 3	MRI	Meteorological Research Institute

where $Q_{\rm net}$ consists of net solar radiation ($Q_{\rm sw}$), upward and downward longwave radiation ($Q_{\rm lw}^{\rm up}$ and $Q_{\rm lw}^{\rm down}$), latent heat flux ($Q_{\rm lh}$), and sensible heat flux ($Q_{\rm sh}$) at surface, and δ denotes the difference between the future and present-day climate state. By Stefan's law, the change of upward longwave radiation at the ocean surface may be approximately written as

$$\delta Q_{\rm lw}^{\rm up} = 4\sigma\overline{T_s}^3\delta T_s, \quad (2)$$

where an overbar denotes the present-day mean state and T_s is the sea surface temperature. Here we assume that the emissivity of ocean surface is unity.

The bulk formulas of surface latent and sensible heat fluxes may be written as

$$Q_{\rm lh} = \rho L C_E V(q_s - q_a) = \rho L C_E V(1 - {\rm RH}e^{-\alpha\Delta T})q_s \quad (3)$$

and

$$Q_{\rm sh} = \rho C_H C_p V(T_s - T_a) = \rho C_H C_p V \Delta T, \qquad (4)$$

where ρ is air density near the surface; C_E and C_H are the heat exchange coefficient of $Q_{\rm lh}$ and $Q_{\rm sh}$, respectively; C_p is the specific heat capacity at constant pressure, V is the surface wind speed, RH is relative humidity, and ΔT is the difference between SST and surface air temperature (i.e., $T_s - T_a$). In a derivation of Eq. (3), the Clausius–Clapeyron equation $\ln(q_{\rm as}/q_s) = -L_v(T_s - T_a)/(RT_sT_a)$ has been applied, where $q_{\rm as}$ is saturated specific humidity of surface air; $\alpha = L_v/RT_sT_a$, where L_v is the latent heat of condensation and R is the ideal gas constant for water vapor. Thus, the change of $Q_{\rm lh}$ with respect to change of SST may be expressed as

$$\delta Q^o_{\rm lh} = \frac{\partial Q_{\rm lh}}{\partial q_s}\frac{\partial q_s}{\partial T_s}\delta T_s = \frac{L_v}{R\overline{T_s}^2}\overline{Q_{\rm lh}}\delta T_s = \gamma_1\overline{Q_{\rm lh}}\delta T_s, \qquad (5)$$

where $\delta Q^o_{\rm lh}$ denotes the part of future surface latent heat flux change due to the SST change. The equation $\delta Q^a_{\rm lh} = \delta Q_{\rm lh} - \delta Q^o_{\rm lh}$ denotes the part of surface latent heat flux change due directly to the change of atmospheric wind speed, relative humidity, and air–sea temperature difference. In Eq. (5), γ_1 is the function of present-day SST field, and for simplicity, it takes a zonal mean value and is only function of latitude, which is about $0.06\,{\rm K}^{-1}$ in the tropics and $0.08\,{\rm K}^{-1}$ in the polar region. Similarly, the future change of $Q_{\rm sh}$ may be decomposed into

$$\delta Q^o_{\rm sh} = \frac{\partial Q_{\rm sh}}{\partial \Delta T}\frac{\partial \Delta T}{\partial T_s}\delta T_s = \rho C_H C_p \overline{V}\frac{\partial \Delta T}{\partial T_s}\delta T_s = \gamma_2\overline{V}\delta T_s \qquad (6)$$

and

$$\delta Q^a_{\rm sh} = \delta Q_{\rm sh} - \delta Q^o_{\rm sh}, \qquad (7)$$

where $\partial\Delta T/\partial T_s$ is empirically determined based on the linear relationship between ΔT and T_s in the present-day climate state, and it is assumed to be only a function of latitude, $\gamma_2 = \rho C_H C_p(\partial\Delta T/\partial T_s)$.

By substituting each of the flux terms above into Eq. (1), one can obtain

$$\delta Q_{\rm sw} - 4\sigma\overline{T_s}^3\delta T_s + \delta Q^{\rm down}_{\rm lw} - \gamma_1\overline{Q_{\rm lh}}\delta T_s - \delta Q^a_{\rm lh} - \gamma_2\overline{V}\delta T_s - \delta Q^a_{\rm sh} + \delta D_0 = 0.$$

Thus, the future change of SST δT_s can be diagnosed by transforming the equation above into

$$\delta T_s = \frac{\delta Q_{\rm sw} + \delta Q^{\rm down}_{\rm lw} - \delta Q^a_{\rm lh} - \delta Q^a_{\rm sh} + \delta D_0}{4\sigma\overline{T_s}^3 + \gamma_1\overline{Q_{\rm lh}} + \gamma_2\overline{V}}. \qquad (8)$$

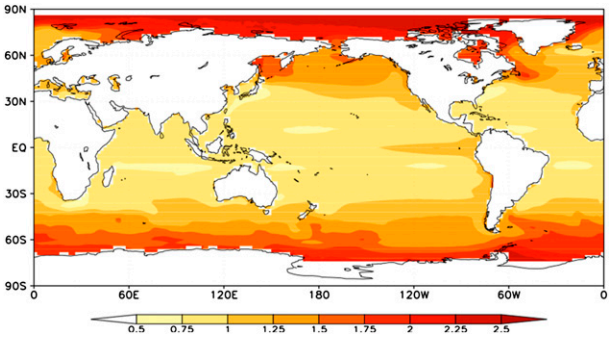

FIG. 2. SST warming pattern (K) predicted by simple analytical model [Eq. (8)] with constant forcing in the numerator ($12\,{\rm W\,m^{-2}}$).

Equation (8) states that the future change of SST is determined by five factors in the numerator: the change of net solar radiation (resulting from the change of cloud and surface albedo), the change of downward longwave radiation (resulting from the change of cloud, greenhouse gases, and air temperature and moisture), the change of surface latent and sensible heat fluxes associated with the change of atmospheric variables such as wind speed and air specific humidity, and the change of oceanic temperature advection. In addition, it is also determined by the denominator, which, as shown later, is primarily controlled by the first two terms that are related to the horizontal distributions of SST and surface latent heat flux in the present-day climate state.

Physically, this simple model represents a surface heat balance between uniform incoming longwave radiative forcing due to greenhouse gases and outgoing longwave radiation and latent heat flux from the surface. In the region where the present-day SST and $Q_{\rm lh}$ are large (small), the balance is achieved with a smaller (larger) increase of SST. This process may be referred to as a "longwave radiative–evaporative damping" mechanism. Consider an idealized climate change scenario in which the atmospheric and oceanic circulations (including clouds as well as temperature gradients) are kept unchanged and downward longwave radiative effect due to greenhouse gases is uniformly distributed. Under such a circumstance, the numerator in Eq. (8) becomes a constant. Because the denominator changes markedly in the meridional direction, one would expect distinctive warming between the tropics and the pole.

Shown in Fig. 2 is an SST warming pattern derived when a constant downward longwave radiative forcing ($\delta Q^{\rm down}_{\rm lw} = 12\,{\rm W\,m^{-2}}$) is specified. Here the value of $\delta Q^{\rm down}_{\rm lw}$ was derived from the ensemble average of the 17 CMIP5 models shown in Table 1, and all other terms in the numerator of Eq. (8) were set to be zero. Note that many features such as the greatest warming in the polar region, an El Niño–like warming pattern in tropical

Pacific, and a greater equatorial than subtropical warming can be explained by this simple analytical model. The pattern correlation coefficient between Fig. 2 and Fig. 1a is 0.7, which is significantly different from zero (exceeds 99% confidence level based on the Student's t test).

Although the two SST warming patterns resemble each other, the magnitudes of the SST changes in Fig. 2 and Fig. 1a are different, indicating that atmospheric feedback also plays a role in determining the actual warming amplitude. The other notable deficiency is that a relatively weak warming in the North Atlantic and the Southern Hemisphere circumpolar region are not captured. As revealed by previous studies (Manabe et al. 1990, 1991), convection in the upper ocean is strong in these two regions, which would transport heat from the surface into a deeper layer and thus cool the ocean surface.

3. Meridional distribution of zonal mean warming pattern

Applying Eq. (8) to the CMIP5 model data, one can diagnose the specific processes that give rise to the zonal mean SST warming pattern shown in Fig. 1b. Figure 3a shows the sum of all five terms in Eq. (8), whereas Fig. 3b shows the contributions from each of the five terms (denoted by a prime to distinguish from the terms in the numerator). The solid black line in Fig. 3a is the SST change obtained from the ensemble average of 17 CMIP5 model projections. The dotted line in Figs. 3a and 3b is future SST change predicted by Eq. (8), with shading representing the spread among these models (here spread is defined as one standard deviation across the models). The simple analytical model predicts the meridional distribution of zonal mean SST change very well. For example, the SST warming over the Arctic Ocean is about 4 times greater than that in the tropics. For the same latitude band, say 60°–75°N versus 60°–75°S, Northern Hemisphere warming is greater.

Figure 3b indicates that the dominant term that determines the meridional distribution of the SST change is $\delta Q_{\rm lw}^{\rm down\prime}$ (green curve). The term $\delta Q_{\rm lh}^{a\prime}$ also contributes to the SST warming, but its effect is mainly confined in the tropics. The term $\delta Q'_{\rm sw}$ is small over tropical and midlatitude regions but somehow contributes to the SST warming in the Arctic Ocean, possibly because of the ice–albedo feedback. The contributions from zonal mean $\delta Q_{\rm sh}^{a\prime}$ and ocean advection are generally small compared to other terms.

The meridional distribution of each numerator (denominator) term is shown in Fig. 3c (Fig. 3d). Note that dominant terms in the denominator are the first two terms. While term $4\sigma\overline{T_s}^3$ depends on present-day SST

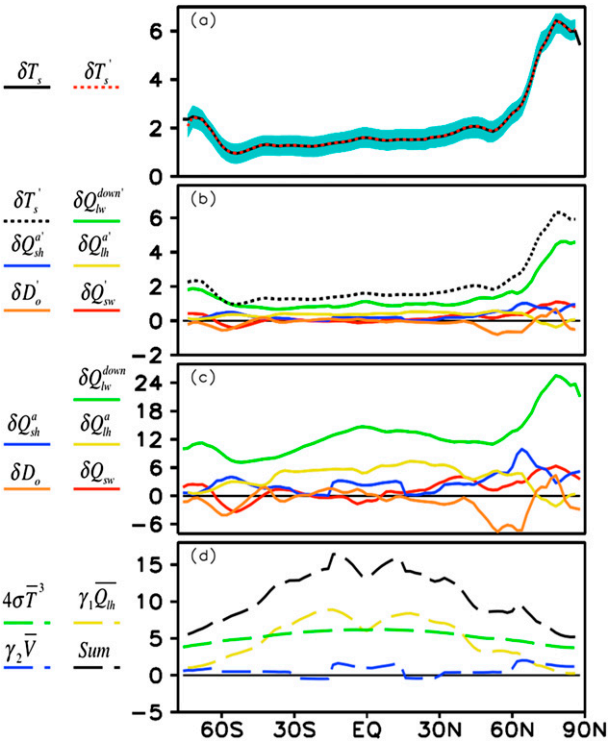

FIG. 3. (a) Zonal mean SST warming profile derived from CMIP5 ensemble (δT_s, black solid line) and predicted by a simple analytical model [Eq. (8)] ($\delta T'_s$, red dotted line). Shading is the uncertainty of $\delta T'_s$ derived from the 17 CMIP5 models. (b) Term $\delta T'_s$ and contributions from each of five terms in the numerator [of Eq. (8)] divided by the denominator, including downward longwave radiation forcing $\delta Q_{\rm lw}^{\rm down\prime}$ (green), sensible heat flux $\delta Q_{\rm sh}^{a\prime}$ and latent heat flux change $\delta Q_{\rm lh}^{a\prime}$ due to change of atmospheric state (blue and yellow), oceanic temperature advection change $\delta D'_0$ (orange), and net solar radiation change $\delta Q'_{\rm sw}$ (red). (c) As in (b), but only for terms in the numerator. (d) Meridional profiles of three terms in the denominator of Eq. (8) and the sum of them (black dashed line) with distribution of present-day mean SST ($4\sigma\overline{T}^3$, green), surface wind speed ($\gamma_2\overline{V}$, blue), and surface latent heat flux ($\gamma_1\overline{Q_{\rm lh}}$, yellow).

distribution, term $\overline{Q_{\rm lh}}$ depends on the meridional distribution of present-day surface latent heat flux. Given that the ratio of the denominator values between the tropics (15°S–15°N) and the Arctic (75°–90°N) is 2.5:1, even a uniform greenhouse radiative forcing would lead to a warming in the Arctic about 2.5 times as large as that in the tropics. This indicates that present-day distribution of $4\sigma\overline{T_s}^3$ and $\overline{Q_{\rm lh}}$ is critical in determining the future warming pattern. The sharp meridional gradient of the denominator is mainly attributed to zonal mean $\overline{Q_{\rm lh}}$ field because of rapid decrease of sea–air specific humidity difference with latitude (Fig. 4). Although the meridional distribution of $4\sigma\overline{T_s}^3$ is relatively uniform, the inclusion of this term greatly reduces the ratio of the denominator between the tropics and the Arctic. The ratio would increase to 15:1 without term $4\sigma\overline{T_s}^3$.

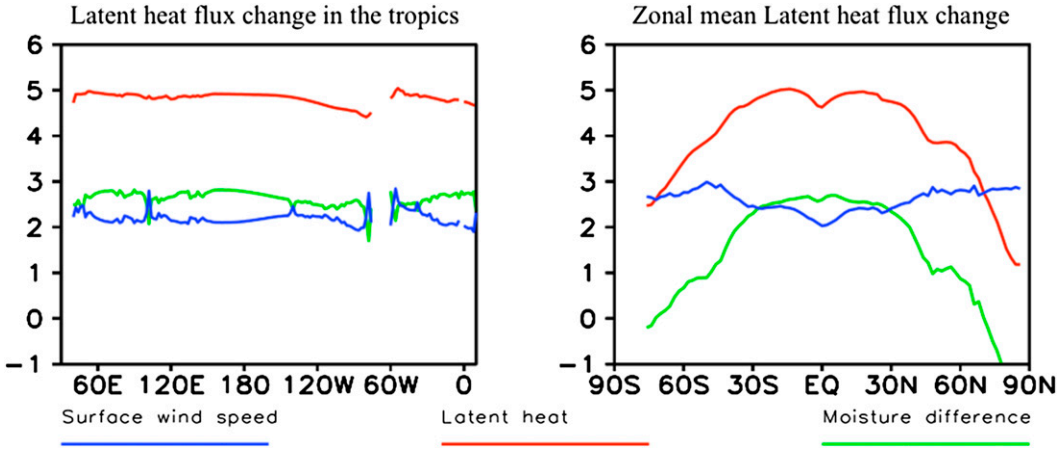

FIG. 4. (left) Zonal distribution of logarithm of the surface latent heat flux in the present-day climate averaged between 5°S and 5°N (red) and the contribution to the heat flux zonal profile by surface wind speed (blue) and air–sea specific humidity difference (green). (right) As in (left), but for zonal mean latent heat flux distribution.

The analysis above implies that about 62.5% of the meridional warming contrast between the Arctic and the tropics is attributed to the meridional distribution of present-day mean SST and surface latent heat flux fields, since the denominator itself can induce 2.5 times greater warming in the polar region when imposed by uniform forcing, while the actual warming is 4 times greater in the polar region. This suggests that the present-day climate state is a major factor in regulating the warming pattern. This is consistent with the fact that all CMIP5 models project a similar meridional warming pattern in Fig. 1b.

In addition, atmospheric longwave radiative feedback (term $\delta Q_{\mathrm{lw}}^{\mathrm{down}}$ in the numerator) further modulates the warming contrast. Figure 3c shows that term $\delta Q_{\mathrm{lw}}^{\mathrm{down}}$ is not uniformly distributed. It peaks in the Arctic Ocean. The ratio of $\delta Q_{\mathrm{lw}}^{\mathrm{down}}$ between the Arctic and the tropics is 1.6:1. This implies that atmospheric feedback can enhance the warming contrast. The cause of the differential $\delta Q_{\mathrm{lw}}^{\mathrm{down}}$ forcing is related to cloud changes in a warmer climate. As shown in Fig. 5, the distribution of clear-sky $\delta Q_{\mathrm{lw}}^{\mathrm{down}}$ is much more uniform compared to Fig. 3c. Thus, the contrast of $\delta Q_{\mathrm{lw}}^{\mathrm{down}}$ between the tropics and the polar region is primarily attributed to greater cloud amount in the polar region under global warming, which traps more $Q_{\mathrm{lw}}^{\mathrm{down}}$ and warms the surface. On the other hand, more clouds also reduce $Q_{\mathrm{sw}}^{\mathrm{down}}$, which partly cancels out positive $\delta Q_{\mathrm{sw}}^{\mathrm{up}}$ associated with sea ice changes and leads to relatively small $\delta Q_{\mathrm{sw}}^{\mathrm{net}}$ in Fig. 3c. While in the clear-sky condition, $\delta Q_{\mathrm{sw}}^{\mathrm{down}}$ is negligible and the distribution of $\delta Q_{\mathrm{sw}}^{\mathrm{net}}$ is dominated by $\delta Q_{\mathrm{sw}}^{\mathrm{up}}$ (Fig. 5). The polar amplification was primarily attributed to sea ice–albedo feedback in previous studies. Here we show that it is attributed to a much smaller $\overline{Q_{\mathrm{lh}}}$ (as well as atmospheric longwave radiative feedback) in the polar region. This result is consistent with previous studies that found a greater polar warming even with no sea ice effect (Alexeev 2003; Alexeev et al. 2005).

It is also noted that there is a hemispheric asymmetry in the SST warming. For instance, the warming over latitude band 60°–75°N is greater than that over 60°–75°S. The difference is primarily caused by the asymmetry in $\delta Q_{\mathrm{lw}}^{\mathrm{down}}$ (Figs. 3c, 5). It is noted that background air temperature in the present-day climate is higher over 60°–75°N than 60°–75°S (Fig. 6). Thus, even with the same air temperature change initially, the resultant $\delta Q_{\mathrm{lw}}^{\mathrm{down}}$ is greater in the northern high-latitude band than the southern counterpart based on Stefan's law. This leads to a greater SST warming in the northern band.

Applying an area integral to Eq. (8), one may estimate the relative roles of atmospheric and ocean feedback processes in determining the global mean SST change (Fig. 7). Note that the ensemble mean of global mean SST warming is 1.7 K, about 65% of which is contributed by $\delta Q_{\mathrm{lw}}^{\mathrm{down}\prime}$.

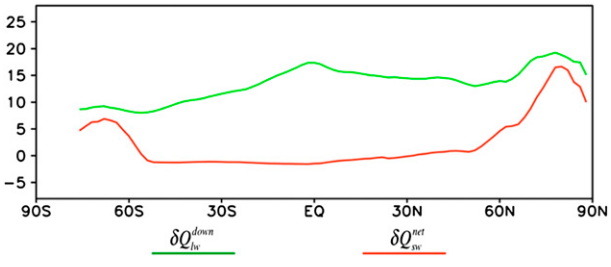

FIG. 5. The distribution of the change of zonal mean clear-sky downward longwave radiation and net solar radiation (global warming minus present day) denoted by green and red lines, respectively (W m^{-2}).

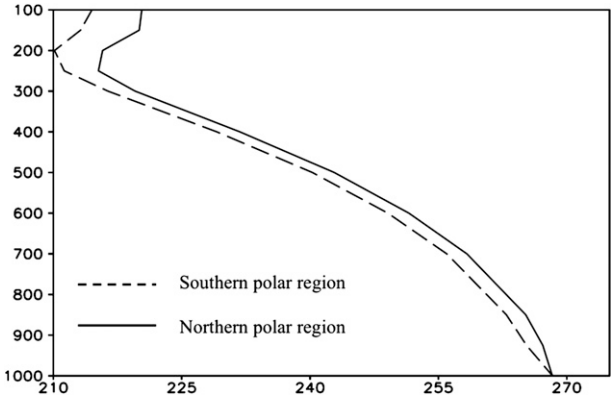

FIG. 6. The vertical profile of area-averaged air temperature (K) in the southern high-latitude region (dashed line, 60°–75°S, zonal mean) and in the northern high-latitude region (solid line, 60°–75°N, zonal mean).

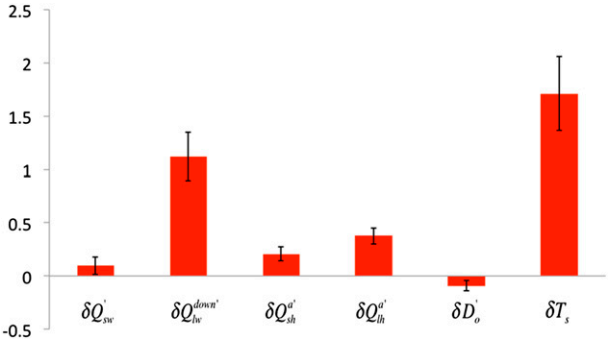

FIG. 7. The area-weighted global mean SST change and the contributions from five terms in Eq. (8) denoted by the red bars. Whiskers show the spread among different CMIP5 models.

4. The SST warming pattern along the equator

One may apply Eq. (8) to the equatorial region (averaged between 5°S and 5°N) to understand the cause of an El Niño–like warming in the Pacific and Atlantic. Figure 8a shows the warming patterns at the equator derived from the ensemble average of 17 CMIP5 models (solid curve) and the simple heat budget model (dashed curve). An El Niño–like pattern in the Pacific and Atlantic and a dipole-like pattern in the IO are well captured.

Among all the atmospheric forcing terms, $\delta Q_{\mathrm{lw}}^{\mathrm{down}\prime}$ again dominates (Fig. 8b). The term $\delta Q_{\mathrm{lh}}^{a\prime}$ also contributes to the equatorial warming, but it acts against SST gradient change in the eastern Pacific and Atlantic. The term $\delta Q_{\mathrm{sh}}^{a\prime}$ is generally small in most regions (Fig. 8b). The term δD_0 favors a La Niña warming pattern, which is consistent with the ocean thermostat mechanism (Clement et al. 1996). The term $\delta Q_{\mathrm{sw}}^{\prime}$ contributes to an El Niño–like warming in both the basins, which is attributed to different cloud responses to surface warming between the east and west of both basins because of different cloud regimes. In the warm pool region, more deep convective clouds would form when the ocean surface becomes warmer (Fig. 9a). In the cold tongue region, low stratus clouds are pronounced because of a stable condition in the lower troposphere associated with trade wind inversion (Philander et al. 1996; Li and Philander 1996). Under global warming, even though the troposphere becomes more stable (Fig. 9b), the subsidence is weakened in the eastern Pacific because of weakened Walker circulation. The competition between the two leads to a small negative cloud change there (Fig. 9a). The distribution of clear-sky $\delta Q_{\mathrm{sw}}^{\mathrm{net}}$ is rather uniform over the equatorial Pacific and Atlantic, which also supports our conclusion that changes of net shortwave radiation in Figs. 8b and 8c are mainly attributed to cloud changes (figure omitted).

Each term of the numerator and denominator in Eq. (8) is shown in Figs. 8c and 8d, respectively. Given that $\delta Q_{\mathrm{lw}}^{\mathrm{down}}$ distributes uniformly over the equatorial Pacific and Atlantic (green curve in Fig. 8c), the El Niño–like warming pattern is attributed to the longwave radiative–evaporative damping mechanism (black dashed line in Fig. 8d). The zonal distribution of the denominator is mainly controlled by the present-day surface latent heat flux ($\overline{Q_{\mathrm{lh}}}$) pattern, which is small in the eastern equatorial

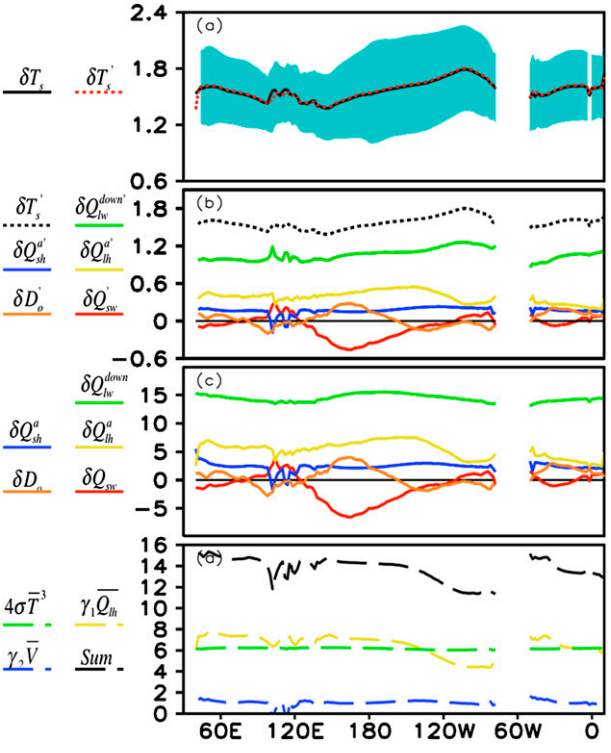

FIG. 8. As in Fig. 3, but for the equatorial region averaged between 5°S and 5°N.

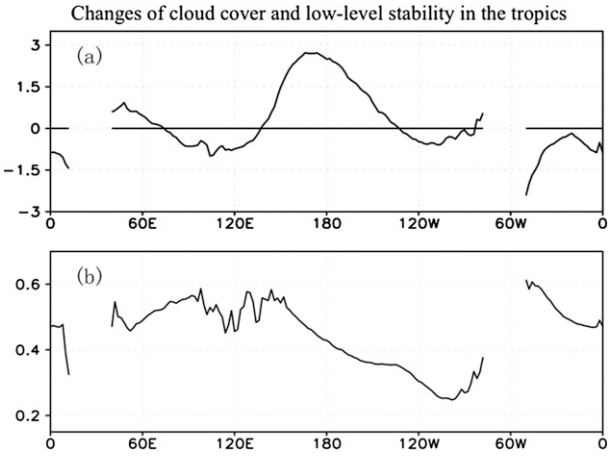

FIG. 9. (a) Ensemble mean cloud cover change (%) and (b) difference between air temperature change at 850 and 1000 hPa ($T_{a\_850\text{hPa}} - T_{a\_1000\text{hPa}}$) (K) averaged within 5°N and 5°S.

Pacific despite a larger surface wind speed there. This again indicates that sea–air specific humidity difference controls the $\overline{Q_{\text{lh}}}$ profile in the Pacific. Term $4\sigma\overline{T_s}^3$ is rather uniform along the equator, and the inclusion of this term in the denominator leads to a weaker warming contrast between east and west of the ocean basins. The result suggests that an El Niño–like warming results essentially from the present-day mean $\overline{Q_{\text{lh}}}$ profile that decreases toward the east in both the Pacific and Atlantic basins.

The formation of the warming pattern in the IO differs from that in the Pacific and Atlantic. Note that in the IO the warming increases toward the west. The westward warming profile is attributed to the effects of $\delta Q_{\text{lw}}^{\text{down}}$, δQ_{lh}^{a}, and δD_0 in the numerator, while the denominator plays a negative role. While a greater value of $\delta Q_{\text{lw}}^{\text{down}}$ in the western IO is associated with increased local moisture and air temperature, the latter two terms in the numerator are related to anomalous low-level easterlies in the equatorial IO in response to the El Niño–like warming in the Pacific (Xie et al. 2010).

5. Conclusions

By constructing a simple heat budget model, we reveal the cause of future SST warming patterns under global warming. We conclude that the most important factor that regulates the meridional distribution of SST warming is the mean SST and latent heat flux profiles in the present-day climate state. In the region where $\overline{Q_{\text{lh}}}$ and $4\sigma\overline{T_s}^3$ are small, it requires a greater ocean warming response to cancel out the imposed longwave radiative forcing. Because of this fundamental feature of the present-day mean climate dependence, all CMIP5 models projected a robust meridional pattern with a much greater warming in the pole than in the tropics. The mean-state induced warming contrast is further amplified by atmospheric longwave radiation feedback associated with cloud changes. The occurrence of an El Niño–like warming in the equatorial Pacific and Atlantic arises from a similar process but with weaker amplitude and a smaller signal-to-noise ratio (Fig. 7). Different cloud feedback in east and west of the two ocean basins also plays a role. The lesser robustness of the east–west warming contrast along the equator than the meridional warming contrast among the models can also be explained by different magnitudes of total denominator contrast. The warming mechanism in the IO, on the other hand, differs markedly from the Pacific counterpart. It is primarily attributed to the remote forcing from the equatorial Pacific through the anomalous Walker circulation.

To sum up, results shown in this study suggest that the global SST warming pattern is mainly controlled by the present-day climate state, although the atmospheric and oceanic feedback might modulate the warming pattern as well. Such conclusions may add confidence to the projection of future SST patterns derived by climate models.

Acknowledgments. This work was supported by China National 973 Project 2015CB453200; NSFC Grant 41475084; ONR Grant N000141210450; the China Scholarship Council (CSC); ARCP2013-27NSY-Liu; and the International Pacific Research Center, which is sponsored by the Japan Agency for Marine-Earth Science and Technology (JAMSTEC). All the datasets from CMIP5 models can be accessed through ESGF data portals (http://pcmdi-cmip.llnl.gov/cmip5/availability.html).

REFERENCES

Alexeev, V. A., 2003: Sensitivity to CO_2 doubling of an atmospheric GCM coupled to an oceanic mixed layer: A linear analysis. *Climate Dyn.,* **20,** 775–787, doi:10.1007/s00382-003-0312-x.

——, P. L. Langen, and J. R. Bates, 2005: Polar amplification of surface warming on an aqua planet in "ghost forcing" experiments without sea ice feedbacks. *Climate Dyn.,* **24,** 655–666, doi:10.1007/s00382-005-0018-3.

Allen, M. R., and W. J. Ingram, 2002: Constraints on future changes in climate and hydrological cycle. *Nature,* **419,** 224–232, doi:10.1038/nature01092.

Clement, A. C., R. Seager, M. A. Cane, and S. E. Zebiak, 1996: An ocean dynamical thermostat. *J. Climate,* **9,** 2190–2196, doi:10.1175/1520-0442(1996)009<2190:AODT>2.0.CO;2.

Held, I. M., and B. J. Soden, 2006: Robust responses of the hydrological cycle to global warming. *J. Climate,* **19,** 5686–5699, doi:10.1175/JCLI3990.1.

Hsu, P., and T. Li, 2012: Is "rich-get-richer" valid for Indian Ocean and Atlantic ITCZ? *Geophys. Res. Lett.,* **39,** L13705, doi:10.1029/2012GL052399.

Knutson, T. R., and S. Manabe, 1995: Time-mean response over the tropical Pacific to increased CO_2 in a coupled ocean–atmosphere model. *J. Climate,* **8,** 2181–2199, doi:10.1175/1520-0442(1995)008<2181:TMROTT>2.0.CO;2.

Li, T., and S. G. H. Philander, 1996: On the annual cycle of the equatorial eastern Pacific. *J. Climate,* **9,** 2986–2998, doi:10.1175/1520-0442(1996)009<2986:OTACOT>2.0.CO;2.

——, M. Kwon, M. Zhao, J.-S. Kug, J.-J. Luo, and W. Yu, 2010: Global warming shifts Pacific tropical cyclone location. *Geophys. Res. Lett.,* **37,** L21804, doi:10.1029/2010GL045124.

Liu, J., B. Wang, M. A. Cane, S. Y. Yim, and J. Y. Lee, 2013: Divergent global precipitation changes induced by natural versus anthropogenic forcing. *Nature,* **493,** 656–659, doi:10.1038/nature11784.

Ma, J., S. P. Xie, and Y. Kosaka, 2012: Mechanisms for tropical tropospheric circulation change in response to global warming. *J. Climate,* **25,** 2979–2994, doi:10.1175/JCLI-D-11-00048.1.

Manabe, S., K. Bryan, and M. J. Spelman, 1990: Transient response of a global ocean-atmosphere model to a doubling of atmospheric carbon dioxide. *J. Phys. Oceanogr.,* **20,** 722–749, doi:10.1175/1520-0485(1990)020<0722:TROAGO>2.0.CO;2.

——, R. J. Stouffer, M. J. Spelman, and K. Bryan, 1991: Transient responses of a coupled ocean–atmosphere model to gradual changes of atmospheric CO_2. Part I: Annual mean response. *J. Climate,* **4,** 785–818, doi:10.1175/1520-0442(1991)004<0785:TROACO>2.0.CO;2.

Murakami, H., and B. Wang, 2010: Future change of North Atlantic tropical cyclone tracks: Projection by a 20-km-mesh global atmospheric model. *J. Climate,* **23,** 2699–2721, doi:10.1175/2010JCLI3338.1.

Philander, S. G. H., D. Gu, D. Halpern, G. Lambert, N.-C. Lau, T. Li, and R. Pacanowski, 1996: Why the ITCZ is mostly north of the equator. *J. Climate,* **9,** 2958–2972, doi:10.1175/1520-0442(1996)009<2958:WTIIMN>2.0.CO;2.

Pithan, F., and T. Mauritsen, 2014: Arctic amplification dominated by temperature feedbacks in contemporary climate models. *Nat. Geosci.,* **7,** 181–184, doi:10.1038/ngeo2071.

Vecchi, G. A., and B. J. Soden, 2007: Global warming and the weakening of the tropical circulation. *J. Climate,* **20,** 4316–4340, doi:10.1175/JCLI4258.1.

——, ——, A. T. Wittenberg, I. M. Held, A. Leetmaa, and M. J. Harrison, 2006: Weakening of tropical Pacific atmospheric circulation due to anthropogenic forcing. *Nature,* **441,** 73–76, doi:10.1038/nature04744.

——, A. Clement, and B. J. Soden, 2008: Examining the tropical Pacific's response to global warming. *Eos, Trans. Amer. Geophys. Union,* **89,** 81–83, doi:10.1029/2008EO090002.

Xie, S.-P., C. Deser, G. A. Vecchi, J. Ma, H. Teng, and A. T. Wittenberg, 2010: Global warming pattern formation: Sea surface temperature and rainfall. *J. Climate,* **23,** 966–986, doi:10.1175/2009JCLI3329.1.

Zhao, M., and I. M. Held, 2010: An analysis of the effect of global warming on the intensity of Atlantic hurricanes using a GCM with statistical refinement. *J. Climate,* **23,** 6382–6393, doi:10.1175/2010JCLI3837.1.

——, and ——, 2012: TC-permitting GCM simulations of hurricane frequency response to sea surface temperature anomalies projected for the late-twenty-first century. *J. Climate,* **25,** 2995–3009, doi:10.1175/JCLI-D-11-00313.1.